



MICROSTRUCTURAL EVOLUTION DURING THE $\alpha_2 \rightarrow \alpha_2 + O$ TRANSFORMATION IN Ti–Al–Nb ALLOYS: PHASE-FIELD SIMULATION AND EXPERIMENTAL VALIDATION

Y. H. WEN^{1,2*}, Y. WANG², L. A. BENDERSKY³ and L. Q. CHEN¹

¹Department of Materials Science and Engineering, The Pennsylvania State University, University Park, PA 16802, USA, ²Department of Materials Science and Engineering, The Ohio State University, 2041 College Road, Columbus, OH 43210, USA and ³Metallurgy Division, NIST, Gaithersburg, MD 20899, USA

(Received 19 August 1999; received in revised form 13 June 2000; accepted 13 June 2000)

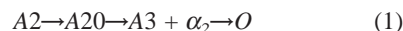
Abstract—The microstructural development during precipitation of a coherent orthorhombic phase (*O*-phase) from an α_2 matrix (DO_{19}) in a Ti–Al–Nb system is investigated through computer simulations using the phase-field approach and through experimental observations using transmission electron microscopy (TEM). Two compositions were considered in the simulations in order to examine the influence of volume fraction of the *O*-phase on the microstructure. It is found that in the alloy with higher volume fraction of the *O*-phase, the precipitates have either square or rectangular shapes on $(0001)_{\alpha_2}$ or $(001)_O$ planes. All the particles are interconnected by sharing their corners. In the alloy with lower volume fraction, the dominant morphology for the precipitates is thin plate. The spatial distribution of precipitates is highly non-uniform with the precipitates aggregating together to form various unique patterns to accommodate the elastic energy arising from the lattice misfit between the α_2 and *O*-phase. All the interfaces between the α_2 and *O*-phase are found to be undistorted habit planes of the type $\{470\}_O$, and the domain boundaries between different orientation variants of the *O*-phase are twin boundaries which are the strain-free planes $\{110\}_O$ or $\{130\}_O$. The simulation predictions agree remarkably well with existing experimental observations and the concurrent TEM study. © 2000 Acta Metallurgica Inc. Published by Elsevier Science Ltd. All rights reserved.

Keywords: Computer simulation; Phase transformations; Precipitation; Ti–Al–Nb alloys; Microstructure

1. INTRODUCTION

Ti–Al–Nb alloys with ~ 10 – 12 and ~ 25 at% Nb have shown very promising combinations of specific strength and rupture life at room and high temperatures (for a general review, see [1]). Phase transformations taking place in these alloys during thermal processing are accompanied by both compositional and structural changes [2], with the latter accompanied by lattice symmetry reduction leading to complex multi-phase and multi-domain microstructures. It is believed that the important physical and mechanical properties of such multi-phase and multi-domain aggregates are determined by the detailed morphology of the multi-domain structures, e.g. the size, shape and spatial arrangement of various orientation

variants of the low-symmetry product phase in the matrix of the high-symmetry parent phase. Extensive experimental studies have been carried out to study the phase equilibria and phase transformation mechanisms in these alloys [3–8]. It is found that the phase equilibria along the Ti_3Al – Nb_3Al pseudo-binary section with Nb < 30 at% involves high temperature phases of BCC-based structures and low temperature phases of hexagonal close-packed structures [9]. Bendersky *et al.* proposed a transformation sequence of Ti–25Al–12.5Nb (at%) alloy upon cooling as



based on the group/subgroup relationship between the parent and product phases [9]. This prediction was supported by their experimental work [10].

Detailed experimental studies were also performed to characterize the orientation relationships, habit planes, domain boundaries and self-accommodating arrangements of different orientation variants of the

* To whom all correspondence should be addressed. Tel.: + 1-614-688-5616; fax: + 1-614-292-1537.

E-mail address: wen@bentley.eng.ohio-state.edu (Y.H. Wen)

O-phase [10–13]. Very complex collective multi-variant domain patterns have been observed. Some of the generic features of the multi-variant domain patterns have been analyzed based on the long-range elastic interactions arising from the lattice mismatch between the parent and product phases as well as between different orientation variants of the product phase. However, these analyses are limited to energetic aspects of the transformations. To understand the formation of these morphological patterns and hence to control the microstructure for desired properties, it is essential to examine the dynamic evolution paths of the domain structures during these phase transformations.

Computer modeling has been proved to be very useful in studying the formation and dynamic evolution of complex microstructures. Some of the generic features of the morphological patterns formed during a congruent hexagonal to orthorhombic transformation have been successfully predicted recently by computer simulations based on a coherent phase-field model [14, 15]. The $\alpha_2 \rightarrow O$ -phase transformation in Ti–Al–Nb is, however, more complicated because both structural and compositional instabilities are involved. For example, the equilibrium microstructural state in the two alloys considered in this paper consists of two coexisting phases of different crystal lattice symmetry and composition. In this case, accommodation of the lattice misfit between the parent and product phases plays an equally important role as the interactions among the different orientation variants of the *O*-phase, and therefore different morphological patterns are expected.

In this paper, we simulate the precipitation processes during coherent $\alpha_2 \rightarrow O$ -phase transformations in two Ti–Al–Nb alloys of different Nb contents which yields different volume fractions of the *O*-phase. The formation and dynamic evolution of the multi-variant and multi-phase microstructural patterns in these alloys are described by a coherent phase field model using experimental data for the major input parameters. Due to the fact that the lattice misfit between the α_2 and *O*-phase normal to (0001) $_{\alpha_2}$ is very small, the two-phase microstructure ($\alpha_2 + O$ -phase) is pseudo-two-dimensional. Parallel rods (or plates in the case of low volume fractions) of the *O*-phase with interfaces normal to the (0001) plane will be formed [12]. Therefore, the microstructural evolution in the system can be effectively modeled in two dimensions on (0001) $_{\alpha_2}$. A parallel experiment is performed to validate the simulation predictions. Excellent agreement between the simulation predictions and experimental observations has been achieved.

2. COMPUTER SIMULATION METHOD

In the phase-field formulation, a multi-phase and multi-variant microstructure is described by a set of conserved and non-conserved field variables. Typical examples are the concentration field which characterizes the composition inhomogeneity, and the long-

range order parameter (*lro*) fields which characterize the structural variation.

To describe the hexagonal to orthorhombic transformation, we need three *lro* parameters, $\eta_1(\mathbf{r}, t)$, $\eta_2(\mathbf{r}, t)$, and $\eta_3(\mathbf{r}, t)$, where \mathbf{r} is the spatial coordinate vector. These *lro* parameters characterize the spatial distribution of three types of structural domains of the *O*-phase with the following orientation relationships: (001) $_O$ //(0001) $_{\alpha_2}$; [100] $_O$ //[2 $\bar{1}$ 10] $_{\alpha_2}$. During the phase transformation, the relaxation of the elastic energy will result in rotation of the *O*-phase necessary to provide invariant plane conditions. A clockwise rotation and a counter-clockwise rotation of a small angle of the three structural domains will produce six orientation variants with new orientation relationships, as has been described by Muraleedharan *et al.* [12]. Therefore, a given *lro* parameter characterizes the spatial distribution of a pair of orientation variants of the *O*-phase corresponding to the clockwise and counter-clockwise rotations. The composition difference between the α_2 and *O*-phase is described by the concentration field, $c(\mathbf{r}, t)$. The spatio-temporal evolution of these variables describes the microstructural evolution. The temporal evolution of the *lro* parameters can be obtained by solving the time-dependent Ginzburg–Landau equation

$$\frac{\partial \eta_p(\mathbf{r}, t)}{\partial t} = -L \frac{\delta F}{\delta \eta_p(\mathbf{r}, t)} + \xi_p(\mathbf{r}, t); p = 1, 2, 3 \quad (2)$$

while the temporal evolution of the concentration field can be described by the non-linear Cahn–Hilliard diffusion equation

$$\frac{\partial c(\mathbf{r}, t)}{\partial t} = M \nabla^2 \frac{\delta F}{\delta c(\mathbf{r}, t)} + \zeta(\mathbf{r}, t) \quad (3)$$

where L and M are kinetic coefficients characterizing structural relaxation and diffusional mobility, F is the total free energy of the system, $\xi_p(\mathbf{r}, t)$ and $\zeta(\mathbf{r}, t)$ are Langvin random noise terms which are related to thermal fluctuations in the *lro* parameter and composition, respectively. They are assumed to be Gaussian distributed and their correlation properties meet the requirements of the fluctuation–dissipation theorem [16].

To present the kinetic equations in an explicit analytical form suitable for a numerical solution, the total free energy F should be expressed as a function of the concentration and *lro* parameter fields. For coherent transformations, the total free energy should consist of two terms: the chemical free energy (F_{ch}) and the elastic strain energy (E_{el}), i.e. $F = F_{\text{ch}} + E_{\text{el}}$.

2.1. Free energy formulation

The non-equilibrium chemical free energy as a function of the field variables can be approximated by the Ginzburg–Landau coarse-grained free energy functional, which contains a local specific free energy, $f(c, \eta_1, \eta_2, \eta_3)$, and gradient energy terms, e.g.

$$F_{\text{ch}} = \int_V \left[\frac{1}{2} \rho (\nabla c)^2 + \frac{1}{2} \lambda \sum_p (\nabla \eta_p)^2 + f(c, \eta_1, \eta_2, \eta_3) \right] dV \quad (4)$$

where ρ and λ are gradient energy coefficients. The integration in equation (4) is carried out over the entire system volume V . As usual, the gradient terms in equation (4) provide an energy penalty to inhomogeneities in composition and lro parameters which take place at interfaces. The local specific free energy $f(c, \eta_1, \eta_2, \eta_3)$ in equation (4) defines the basic thermodynamic properties of the system. It can be approximated either by a Bragg–William-type of mean-field model or by a Landau-type polynomial expansion. In this paper, the latter is adopted. In principle, the polynomial may include any terms allowed by the symmetry operations with respect to the parent phase [17]. For example, for the hexagonal to orthorhombic ordering transformation considered in [14], an expansion up to the sixth order in the lro parameters contains quadratic, fourth, and sixth-order terms. In this work, we employ a similar model, i.e.

$$f(c, \eta_1, \eta_2, \eta_3) = \frac{A_1}{2} (c - c_1)^2 + \frac{A_2}{2} (c_2 - c) \sum_p \eta_p^2 - \frac{A_3}{4} \sum_p \eta_p^4 + \frac{A_4}{6} (\sum_p \eta_p^2)^3, \quad (5)$$

where c_1 and c_2 are constants close to the equilibrium compositions of the parent α_2 and product O -phase, respectively. A_1 – A_4 are positive constants. A similar free energy model has been used for the cubic to tetragonal transformation [18, 19]. Minimization of the local free energy given in equation (5) with respect to both composition and lro parameter yields a two-phase equilibrium with three pairs of orientation variants for the O -phase because the free energy functional has three degenerated minima corresponding to the three lro parameters. A conven-

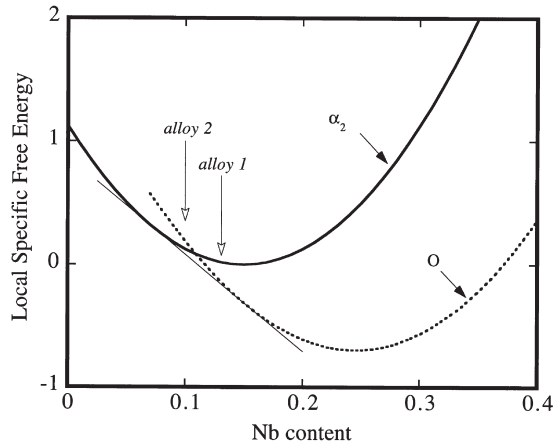


Fig. 1. Local specific free energy for parent and product phases as a function of the content of Nb.

tional free energy versus composition plot can be obtained by minimizing the free energy with respect to the lro parameter and then substituting the equilibrium lro parameter as a function of composition back into the free energy expression (see e.g. Fig. 1).

The elastic strain energy as a function of the lro parameters associated with a coherent hexagonal to orthorhombic transformation has been derived in [14, 15] based on the linear elasticity theory of Khachaturyan [20]. The final form of the total elastic energy of a multi-variant and multi-phase mixture can be expressed as

$$E_{\text{el}} = \frac{V}{2} C_{ijkl} \bar{\epsilon}_{ij} \bar{\epsilon}_{kl} - VC_{ijkl} \bar{\epsilon}_{ij} \sum_p \epsilon_{kl}^0(p) \overline{\eta_p^2(\mathbf{r})} + \frac{V}{2} C_{ijkl} \sum_p \sum_q \epsilon_{ij}^0(p) \epsilon_{kl}^0(q) \frac{\overline{\eta_p^2(\mathbf{r}) \eta_q^2(\mathbf{r})}}{\eta_p^2(\mathbf{r}) \eta_q^2(\mathbf{r})} - \frac{1}{2} \sum_{p=1}^3 \sum_{q=1}^3 \int \frac{d^3 \mathbf{g}}{(2\pi)^3} B_{pq}(\mathbf{n}) \{ \eta_p^2(\mathbf{r}) \}_{\mathbf{g}}^* \{ \eta_q^2(\mathbf{r}) \}_{\mathbf{g}} \quad (6)$$

where $\overline{(\dots)}$ represents the volume average of (\dots) , V is the total volume of the system, C_{ijkl} is the elastic moduli tensor. ϵ is the elastic strain tensor, and $\epsilon^0(p)$ is the stress-free transformation strain tensor for variant p which was defined in equation (14) of [15]. $B_{pq}(\mathbf{n})$ is a two-body interaction potential given by

$$B_{pq}(\mathbf{n}) = n_i \sigma_{ij}^0(p) \Omega_{jk}(\mathbf{n}) \sigma_{kl}^0(q) n_l \quad (7)$$

where $\mathbf{n} = \mathbf{g}/g$ is a unit vector in reciprocal space and n_i is its i th component, $\sigma_{ij}^0(p) = C_{ijkl} \epsilon_{kl}^0(p)$ and $\Omega_{ij}(\mathbf{n})$ is a Green function tensor which is inverse to the tensor $\Omega_{ij}^{-1}(\mathbf{n}) = C_{ijkl} n_k n_l$,

$\{ \eta_q^2(\mathbf{r}) \}_{\mathbf{g}} = \int \frac{d^3 \mathbf{g}}{(2\pi)^3} \eta_q^2(\mathbf{r}) \exp(-i\mathbf{g} \cdot \mathbf{r})$ is the Fourier transform of $\eta_q^2(\mathbf{r})$ and $\{ \eta_p^2(\mathbf{r}) \}_{\mathbf{g}}^*$ is the complex conjugate of $\{ \eta_p^2(\mathbf{r}) \}_{\mathbf{g}}$. The readers are referred to [14, 15] for more details.

The first two terms on the right-hand side of the above equation describe the elastic energy due to a homogeneous deformation. The third term describes the elastic energy associated with deforming the stress-free product phase back into its geometrical shape before the transformation, and the last term describes the heterogeneous relaxation of the precipitates which does not produce any macroscopic shape change but affects the shape, size and spatial distribution of the product phase. In this work, the macroscopic homogeneous strain $\bar{\epsilon}_{ij}$ is assumed to be zero which corresponds to a system of a single grain embedded in a poly-crystal material. As a result, the first two terms vanish.

2.2. Normalization of the kinetic equations and choice of the phenomenological parameters

For the convenience of numerical solution, the kinetic equations are transformed into dimensionless form through the introduction of a reduced time, defined as $\tau = L|\Delta f|t$, and reduced spatial coordinates, defined as $u_i = x_i/l$. In these definitions, $|\Delta f|$ is the chemical driving force for the phase transformation under consideration and l is the length unit of the computational grid size. Substituting these reduced variables into equations (4)–(6), we get the dimensionless form of the kinetic equations:

$$\frac{\partial \eta_p(\mathbf{u}, \tau)}{\partial \tau} = - \left(-\beta \nabla^2 (\eta_p(\mathbf{u}, \tau)) + \frac{\partial f_a}{\partial \eta_p(\mathbf{u}, \tau)} + \phi \frac{\delta E'_{cl}}{\delta \eta_p(\mathbf{u}, \tau)} \right) + \xi'_p(\mathbf{u}, \tau) \quad (8)$$

$$\frac{\partial c(\mathbf{u}, \tau)}{\partial \tau} = \vartheta \nabla^2 \left(-\alpha \nabla^2 c(\mathbf{u}, \tau) + \frac{\partial f_a}{\partial c(\mathbf{u}, \tau)} \right) + \zeta'(\mathbf{u}, \tau) \quad (9)$$

where

$$\phi = \frac{4G\epsilon_s^2}{|\Delta f|}, \beta = \frac{\lambda}{l^2|\Delta f|}, \quad (10)$$

$$\vartheta = \frac{M}{Ll^2}, \alpha = \frac{\rho}{|\Delta f|l^2} \quad (11)$$

$$f_a = \frac{a_1}{2}(c - c_1)^2 + \frac{a_2}{2}(c_2 - c) \sum_p \eta_p^2 - \frac{a_3}{4} \sum_p \eta_p^4 + \frac{a_4}{6} \left(\sum_p \eta_p^2 \right)^3 \quad (12)$$

where G is the shear modulus, $a_i = \frac{A_i}{|\Delta f|}$, $i = 1, 2, 3, 4$;

and $\xi'_p(\mathbf{u}, \tau) = \frac{\xi_p(\mathbf{r}, t)}{L|\Delta f|}$; $\zeta'(\mathbf{u}, \tau) = \frac{\zeta(\mathbf{r}, t)}{L|\Delta f|}$;

$$\frac{\delta E'_{cl}}{\delta \eta_p(\mathbf{u}, \tau)} = \frac{2\eta_p(\mathbf{u}, \tau)}{4G\epsilon_s^2} \left(-C_{ijkl}\epsilon_{ij}\epsilon_{kl}^0(p) + \sum_{q=1}^3 \langle C_{ijkl}\epsilon_{ij}^0(p)\epsilon_{kl}^0(q)\eta_q^2(\mathbf{u}, \tau) - \{B_{pq}(\mathbf{n})\{\eta_q^2(\mathbf{u}, \tau)\}_{\mathbf{g}'}\}_{\mathbf{u}} \rangle \right),$$

where $\mathbf{g}' = \mathbf{g}l$.

The solution of the field kinetic equations

(equations (8) and (9)) is determined by the four dimensionless parameters, i.e. ϕ , β , α and ϑ . The parameters ϕ , β and α characterize the magnitudes of specific strain energy and gradient energies with respect to the chemical driving force. In our simulation, ϕ , β and α have been assumed to be 35, 0.05 and 0.0, respectively. By assuming $\alpha = 0.0$, we neglect the gradient energy effect due to compositional inhomogeneity in solving the Cahn–Hilliard diffusion equation. This implies that the diffusion is described by a non-linear diffusion equation while the interfacial energy is introduced by the gradient terms in the long-range order parameter fields only. ϑ is assumed to be 1.0.

Those phenomenological polynomial expansion coefficients in equation (12) should be chosen properly to provide a qualitatively correct description of the specific free energy of the system. Although an accurate phase diagram of the system and the free energy curves of α_2 and O -phase are not available at the present time, we have chosen $(a_1, a_2, a_3, a_4, c_1, c_2) = (100.0, 24.0, 22.0, 27.8, 0.15, 0.245)$ to fit the estimation of the free energy curves given by Bendersky *et al.* (see Fig. 18 in [10]) based on their experimental work. The local free energy minima defined by equation (12) with the above chosen parameters are projected onto the f - c plane and plotted in Fig. 1. It shows two branches, one describing the α_2 phase and the other describing the O -phase. As can be seen, it reproduces what was estimated by Bendersky *et al.* (see Fig. 18 in [10]). It should be noted that the accuracy of the specific free energy is not critical as long as the sequence of the morphological transformation rather than the quantitative values of the transformation rate is concerned.

3. SIMULATION RESULTS

All the simulations are carried out on a two dimensional (2D) unit cell with 1024×1024 mesh points. Equations (8) and (9) are solved numerically in the Fourier space using a semi-explicit algorithm [21]. Assuming that the microstructure is macroscopically homogeneous, we can apply periodical boundary conditions along both dimensions. The spatial and time increment in our numerical solution have been chosen as $du_x = du_y = 0.125$ and $d\tau = 0.02$.

The initial condition for the simulation is a homogeneous α_2 phase described by

$$c(\mathbf{r}) = \bar{c}; \eta_1(\mathbf{r}) = 0, \eta_2(\mathbf{r}) = 0, \eta_3(\mathbf{r}) = 0;$$

where \bar{c} is the mean Nb composition of the alloy. As indicated by the common tangent in Fig. 1, the equilibrium composition for the two coexisting phases are $\sim 7\%$ (for the α_2 phase) and $\sim 15\%$ Nb (at%) (for the O -phase). Two alloys with $\bar{c} = 12.5$ at% (corresponds to Alloy 1 in Fig. 1) and $\bar{c} = 10$ at% Nb (Alloy 2 in Fig. 1) are considered in this work. In the

absence of coherent stress, the equilibrium volume fractions of the O -phase in the two alloys are 69 and 37%, respectively.

According to the local specific free energy curve in Fig. 1 with the phenomenological parameters specified in Section 2.2, the initial hexagonal phase is metastable. The transformation takes place through a nucleation and growth mechanism. In the simulations, the nucleation process is simulated through the noise terms in the kinetic equations (8) and (9) which result in local fluctuations in concentration and lro parameters leading to nucleation of the O -phase.

The simulated microstructural evolution during isothermal aging of Alloy 1 is shown in Fig. 2. The shades of gray in the simulated micrographs represent the values of $(\eta_1^2 + \eta_2^2 + \eta_3^2)$, e.g. the higher the value, the brighter the shade. Therefore, the white areas represent the O -phase and the black background represents the α_2 phase. At the reduced time $\tau = 4$ (Fig. 2(a)), many precipitates of the O -phase have appeared. Then the noise terms in the kinetic equations were turned off. Further evolution of the microstructure is controlled by growth and coarsening (Fig. 2(b–d)). At $\tau = 40$ (Fig. 2(b)), most of the O -phase precipitates have rectangle/square shapes and their spatial arrangements form some unique patterns. This

becomes more evident in later stages as shown in Fig. 2(c) and (d). Most of the rectangles and squares are connected at their corners. In the upper left corner of Fig. 2(c), one can find some nearly perfect hexagons of the parent α_2 phase surrounded by the variants of the O -phase which are connected at their corners and are evenly spaced. Some other regular patterns can also be found depending on how the variants of the O -phase come into contact.

To better identify and understand these patterns we need to distinguish the three pairs of orientation variants of the O -phase. For this purpose, we recast the result shown in Fig. 2(d) by a different plotting scheme (Fig. 3) where the shades of gray represent the values of $(\eta_1^2 - \eta_2^2 - 2 \times \eta_3^2)$. Accordingly, four different shades of gray correspond to pair one, parent α_2 phase, pair two, and pair three, respectively, with decreasing brightness. Our simulation demonstrates that in those areas where only two orientation variants of the O -phase are present, the rectangular and square shaped precipitates form a chess-board pattern (refer to the area enclosed by a dashed circle and the basic element of the pattern shown in Fig. 4(a)) which is very similar to the microstructure obtained by Bouar *et al.* for the cubic \rightarrow tetragonal transformation in a Co–Pt alloy in their numerical and experimental stud-

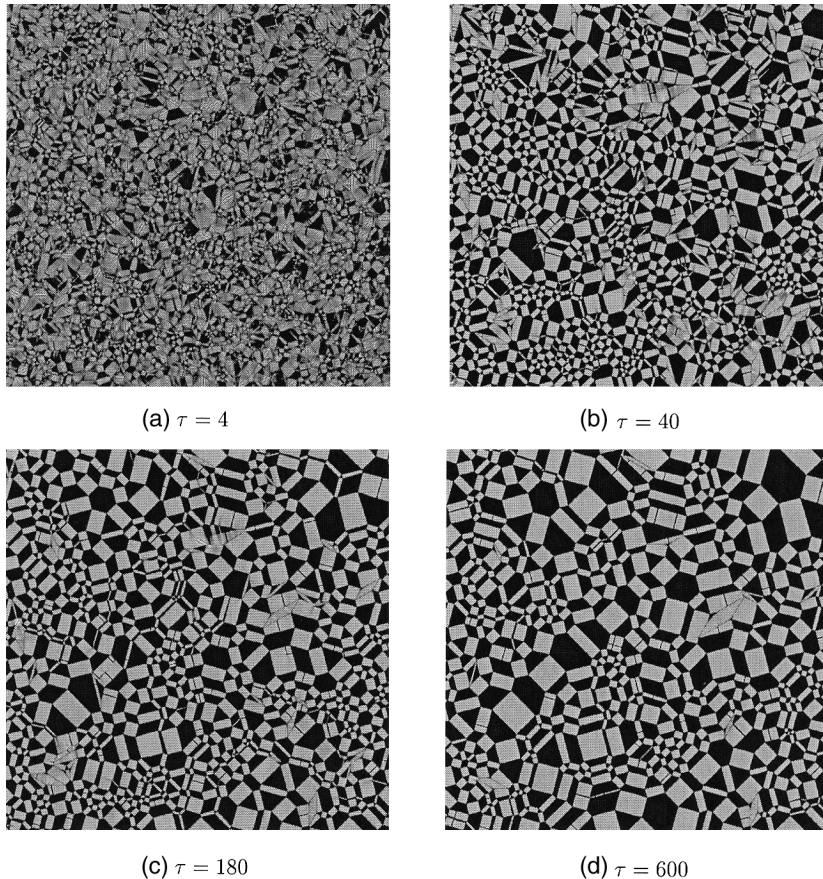


Fig. 2. Simulated precipitation process of orthorhombic domains from a hexagonal matrix started from the nucleation stage.

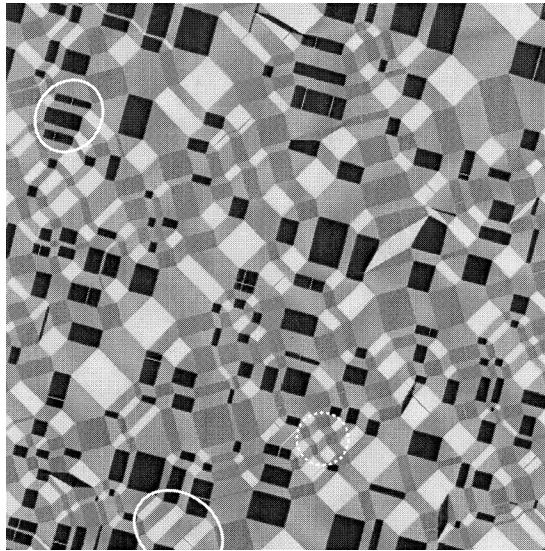


Fig. 3. Recast of microstructure shown in Fig. 2(d) to distinguish three pairs of orientation variants of the O -phase. The chess-board-like structure can be found in an area enclosed by a dashed circle where only two orientation variants of the O -phase are present. Enclosed in the white ellipses are some parallel striations of alternating $\alpha_2 + O$.

ies [22]. Since there are only two orientation variants in their 2D simulations of the cubic \rightarrow tetragonal transformation, the chess-board structure is the only pattern observed. In the current simulation, however, there are three pairs of orientation variants and more complex morphological patterns are formed. For example, when three or more variants are present, four different kinds of morphological patterns have been found in our simulation, as illustrated in Fig. 4(b–e). There are also some parallel striations of alternating α_2 and O -phase (refer to those areas enclosed in white ellipses in Fig. 3). These patterns are unique for a two-phase mixture of the α_2 and O -phases and were not found in the single phase multi-variant mixture produced by a congruent transformation from hexagonal to orthorhombic in our previous simulation studies [14, 15]. In these patterns, the α_2 parent phase particles enclosed by the O -phase precipitates assume different shapes including triangles, trapezia, irregular pentagons, or hexagons with included angles in multiples of 60° . The final microstructure shown in Fig. 2(d) consists of various combinations of these basic patterns.

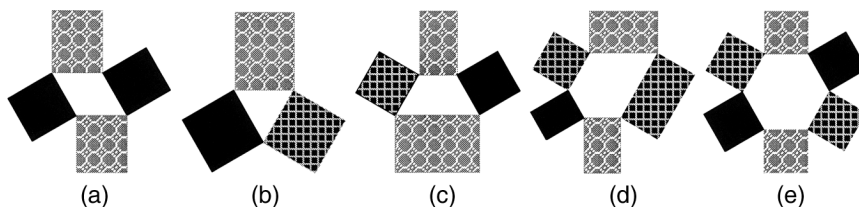


Fig. 4. Schematic simulated patterns where different filling patterns are employed to represent three pairs of orientation variants of the O -phase. The central untransformed α_2 phase assume different shapes including triangles, trapezia, irregular pentagons, or hexagons with included angles in multiples of 60° .

The simulated microstructural evolution during precipitation in Alloy 2 with 10.0 at%Nb is shown in Fig. 5. The shades of gray are the same as those employed in Fig. 3. In this simulation, the noise terms were also turned off at $\tau = 4$. The particles of the O -phase formed at this moment are illustrated in Fig. 5(a). Further growth and coarsening of the O -phase particles lead to some unique patterns which are enclosed by dashed ellipses in Fig. 5(b). These patterns are summarized in Fig. 6. Some of them are similar to what have been summarized in Fig. 4, but the dominant morphology of precipitates is thin plate in Fig. 5(b) in contrast to that of rectangle/square found in Fig. 2. This difference can be attributed to the fact that there is less interference among the three pairs of variants in the current case with lower volume fraction of the O -phase. As we have demonstrated before [15], a single variant without interference from other variants always forms a thin plate of well-defined habit plane as a result of minimizing the associated elastic energy.

The spatial distribution of precipitates is rather inhomogeneous. In areas where more precipitates are present (see those areas highlighted by white circles in Fig. 5(b)), one can find that the dominant particle shapes for the O -phase are rectangle/square which are essentially the same as those described earlier in Fig. 2 with higher volume fraction of the O -phase. However, these kind of structures are unstable against coarsening due to the fact that they have more interfaces and the elastic energy associated with the structures is also higher than that associated with a thin plate. For example, the precipitates enclosed in the lower white circle in Fig. 5(b) almost completely disappeared at a later stage at $\tau = 180$ (Fig. 5(c)). The precipitates enclosed in the upper white circle in Fig. 5(b) also disappeared at $\tau = 600$ (Fig. 5(d)). As a result, one can hardly find precipitates of rectangle/square shapes in the final microstructure shown in Fig. 5(d) after a relatively long period of coarsening.

It is interesting to note that strong particle rearrangement takes place during the coarsening process. One example is the alignment of two black plates enclosed in the solid ellipse in Fig. 5(c) as compared to its configuration at earlier stages (e.g. Fig. 5(b)). As a result, a very regular pattern is formed. In another area of Fig. 5(c) (enclosed by a dashed

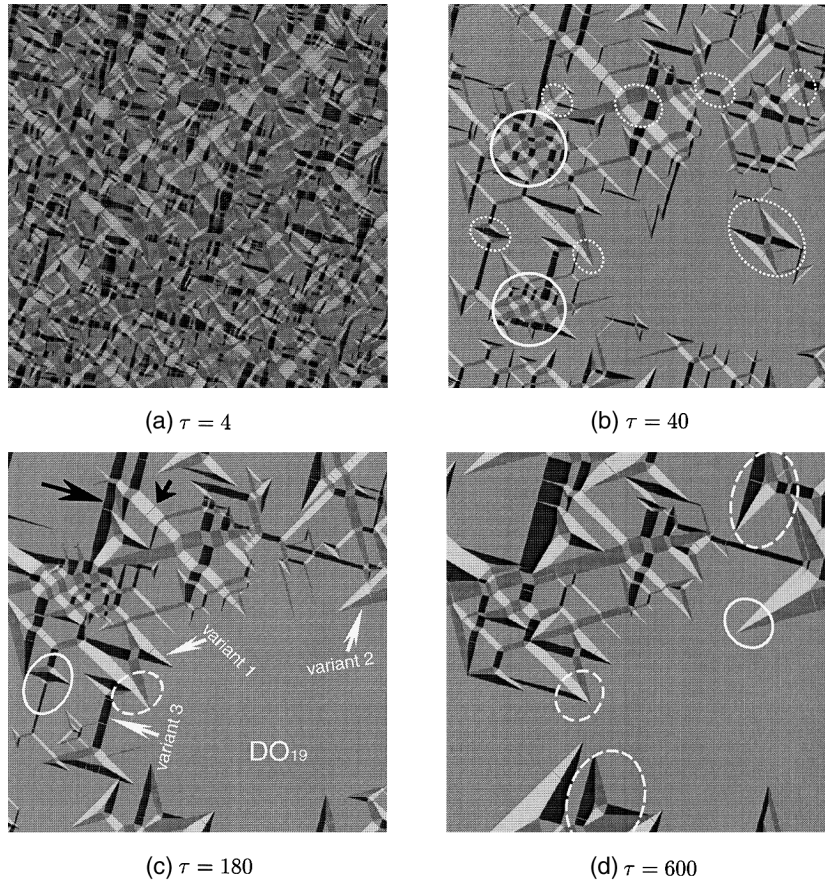


Fig. 5. Simulated precipitation process with 10.0 at%Nb as the mean composition of the Ti–Al–Nb alloy. Microstructural patterns enclosed by dashed ellipses in (b) and (d) are to be compared with experimental observations. The shades of gray representing the parent α_2 and the three pairs of orientation variants of the O -phase are indicated in (c).

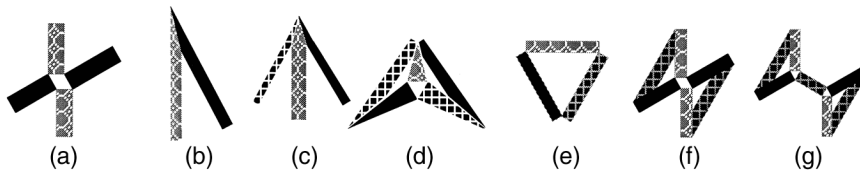


Fig. 6. Schematic simulated patterns with relatively low volume fraction of O -phase in an α_2 matrix. Both domain/domain and domain/matrix interfaces are involved.

ellipse), a spear-like pattern formed by two different variants is in contact with a black variant from a pattern below. With further coarsening, we found that the pattern below disappeared (Fig. 5(d)) leaving the black variant joining the spear-like pattern and converting it into another regular pattern as shown in Fig. 6(c). This pattern was observed by Muraleedharan and Banerjee [12]. They have suggested that this kind of pattern is most likely formed by nucleation of a third variant at the junction of two existing variants because it is unlikely that three plates could have terminated at the same point. Our dynamic simulation suggests that nucleation of a third variant is not necessary for the formation of this particular pattern,

i.e. the pattern can simply emerge during the coarsening process.

During the coarsening process, most precipitates show simple scaling. Following the dynamic evolution of some individual variants/patterns, e.g. the black and white variants indicated by black arrows in Fig. 5(c) and the spear-like pattern enclosed by the solid ellipse in Fig. 5(d), one can find significant plate thickening (thinning) and domain coarsening took place between $\tau = 180$ and $\tau = 600$.

4. EXPERIMENTAL VALIDATION AND DISCUSSION

Our computer simulations performed without any *a priori* assumption on the possible geometry of the

microstructure have revealed some very interesting morphological patterns for the two-phase and multi-variant coherent mixture of Ti–Al–Nb alloys. The morphology and mutual arrangement of the O -phase are very different from those predicted for the hexagonal→orthorhombic congruent ordering [14, 15] where the equilibrium state is a single-phase multi-variant coherent aggregate. In addition, the volume fraction of the O -phase has been shown to have a strong influence on the domain structure formed. To validate these predictions, in the following we compare our simulation results with experimental observations and discuss the mechanisms underlying the formation of those basic motifs shown in Figs 4 and 6.

Experimental study of the transformation is performed by TEM on an alloy with a composition Ti–31.25Al–18.75Nb (at%). In this alloy α_2 precipitates first form in a B2 matrix at 1373 K, with the compositions of the α_2 and B2 phases being Ti–29Al–15Nb (at%) and Ti–34.5Al–14Nb (at%), respectively. Annealing of this alloy at 973 ~ 1073 K results in further decomposition of the α_2 phase into a two-phase mixture of $\alpha_2 + O$ -phase. As one may have noticed, the alloy composition is not exactly the same as either of those that we employed in our simulation and the phase transformation path is more complicated. However, the volume fraction of the O -phase within the α_2 phase is found to be similar to that in Alloy 2 chosen in the simulation. In addition, the interfaces between α_2 and O -phase are found to be coherent. In the simulation, we have employed the same lattice parameters for the equilibrium α_2 and O -phase found in the experiment. Therefore, the experimental observations can be employed to validate our predictions.

To compare the experimental observation with the simulation predictions, we need to examine the microstructure in the direction of the c -axis of the hexagonal phase. In this orientation diffraction patterns of the α_2 and O -phase are different only by a small difference in lattice parameters, and therefore it is extremely difficult to identify different variants from selected area or microdiffraction patterns (Fig. 7). In our microstructural analysis we use orientations of domain boundaries and α_2/O -phase interfaces to identify the α_2 matrix and three pairs of variants of the O -phase. We assumed that the inter-phase and inter-variant interfaces are strain-free coherent habit planes, with orientations dictated by lattice mismatch and symmetry relationship, respectively. The expected orientations of the habit planes are shown in Fig. 7(b) and (c), where the strain-free α_2/O -phase interfaces are calculated to be approximately $\{470\}_O^*$ using the following orthorhombic lattice parameters:

α_2 : $a = 0.59$ nm, $b = 0.985$ nm, $c = 0.465$ nm; O -phase: $a = 0.609$ nm, $b = 0.957$ nm, $c = 0.465$ nm.

Fig. 8 shows an example of a transformed precipitate in the alloy annealed at 1373 K (to form α_2) and then at 1123 K. The precipitate has an envelope of an inter-diffusion zone where the α_2 transforms to the O -phase. The interior of the precipitate has undergone the $\alpha_2 \rightarrow \alpha_2 + O$ decomposition where three pairs of variants of the O -phase coexist with the α_2 matrix.

Examples of different microstructural patterns involving interaction between two or more variants of the O -phase in the α_2 matrix observed in the experiment are shown in Fig. 9. Fig. 9(a) shows impingement between two variants leading to a spear-like pattern with a twin interface between them. In Fig. 9(b), one can find that the thickness of variant 2 is affected by the contact of variant 1 which is very similar to what has been predicted by our simulation (compare it with the pattern enclosed by the white dashed ellipse in Fig. 5). Fig. 9(c) shows a pattern of two intersecting variants with an island of the matrix phase at the intersection. Such a configuration is the most frequently observed pattern in this alloy. Fig. 9(d–f) shows some patterns consisting of more variants. All these patterns agree very well with those predicted in our simulation as shown in Fig. 6.

Muraleedharan *et al.* [11, 12] have also studied the morphology and spatial distribution of the O -phase in Ti–Al–Nb alloys. They have identified a composition range and a heat treatment schedule with which an isothermal decomposition of the α_2 into a two-phase mixture of α_2 and O -phase takes place without intervention of the β phase. They investigated the morphologies and distribution of the O -phase at various aging temperatures ranging from 1173 to 673 K. The aging temperature was shown to have a significant influence on the volume fraction of the O -phase. The volume fractions of the O -phase formed at the aging temperatures of 1173 and 1073 K are comparable with those in the two alloys presented in Section 3. In the following, these results are compared to our simulation predictions.

On aging at 1173 K, which produces a relatively low volume fraction of the O -phase, the experimental observations show that the morphology of the O -phase precipitate is also thin plate and the mutual arrangement of these plates forms some intersection in multiples of 30° with respect to each other (Figs 7, 8, 10 and 11 in [12]), which agrees remarkably well with those predicted by our simulations (Figs 5 and 6).

On aging at 1073 K, which produces a relatively high volume fraction of the O -phase (see Fig. 3 in [11]), the initial microstructures contain some fine scale domain structures as a result of the decomposition. These domains develop into “mosaic” patterns during the growth and coarsening process. The mosaic patterns are composed of alternating α_2 and O -phase platelets which are similar to what we predicted. For example, there are many substructures of

* $\{470\}$ means that the first two numbers can be permuted and have their signs changed but the third number is specific.

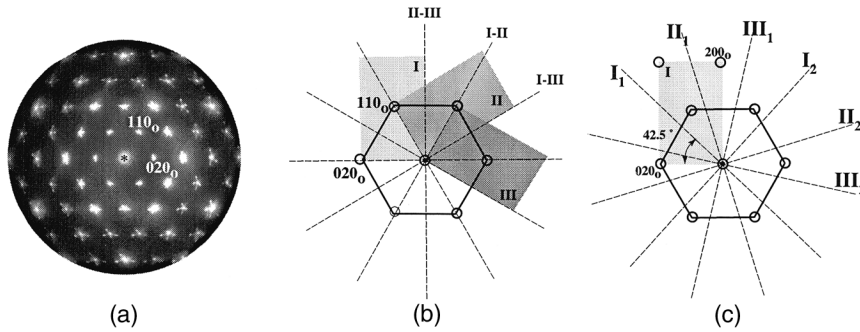


Fig. 7. (a) Selected area diffraction pattern from an area where all three pairs of variants of the O -phase and the α_2 matrix are present; (b) domain/domain interfaces along $\{110\}_O$ or $\{130\}_O$ where I, II, and III represent the three pairs of structural variants of the O -phase. Interface between two variants, say variant I and II, is illustrated by I-II; and (c) domain/matrix interfaces along $\{470\}_O$ where I_1 and I_2 correspond to two near-orthogonal strain-free interfaces of variant I with the matrix.

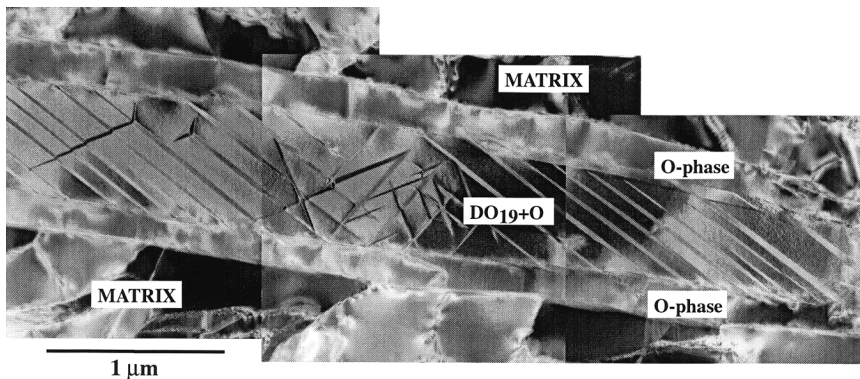


Fig. 8. TEM image of a precipitate in the alloy annealed at 1373 K and then at 1123 K for 77 h. The precipitate has an envelope of inter-diffusion zone where 100% O -phase was formed. Interior of the precipitate undergoes the $\alpha_2 \rightarrow \alpha_2 + O$ decomposition.

parallel striations of alternating α_2 and O -phase in the experimental observation (Fig. 3 in [11]). In Fig. 3, one can also find this kind of microstructural pattern (refer to those areas enclosed in white ellipses). In addition, our simulations have predicted some other microstructural features consisting of the basic patterns illustrated in Fig. 4. In our parallel experimental study carried out in an alloy with comparable volume fraction of the O -phase, we have observed the chess-board-like structure (see the central part of Fig. 10). Similar patterns can be easily identified in Fig. 3. However, microstructural patterns based on some other basic motifs, e.g. (b–e) shown in Fig. 4, have not been observed yet in the existing experimental studies. Further validation from experimental studies is desirable.

Further lowering the aging temperature to 973 K, a completely different microstructural pattern emerges (Fig. 11(a)). While alternating $\alpha_2 + O$ can still be found in some areas, the microstructure is mainly composed of colonies consisting solely of the three pairs of variants of the O -phase, which indicates that the aging at 973 K has resulted in an even higher volume fraction of the O -phase. To test the influence of a very high volume fraction of the O -phase on the

microstructural pattern, we have carried out an additional simulation with the mean composition of Nb being 25.0 at%, with which the alloy is situated in a congruent transformation regime (refer to Figs 1 and 12). In Fig. 11(b), we show the corresponding microstructure formed at the final stage of the simulation. The shades of gray are the same as those employed in Fig. 5 but here there is no retained α_2 phase. The microstructure shown in Fig. 11(b) is completely different from those shown earlier in Figs 2 and 5. The dominant morphology for a single variant is diamond-like which is what has been observed in Fig. 11(a). The spatial arrangement among different variants forms various patterns, e.g. a star pattern enclosed by a black ellipse in Fig. 11(b) which is very similar to the experimentally observed one enclosed by a white ellipse in Fig. 11(a).

In our previous work dealing with congruent hexagonal to orthorhombic transformation [15], we calculated the habit plane orientations for the three pairs of orientation variants of the O -phase. Each of these habit planes actually corresponds to an invariant plane strain condition (or strain-free interface) which can be obtained by simple calculations [20, 23]. As shown in Fig. 7(c), one can find that those invariant planes

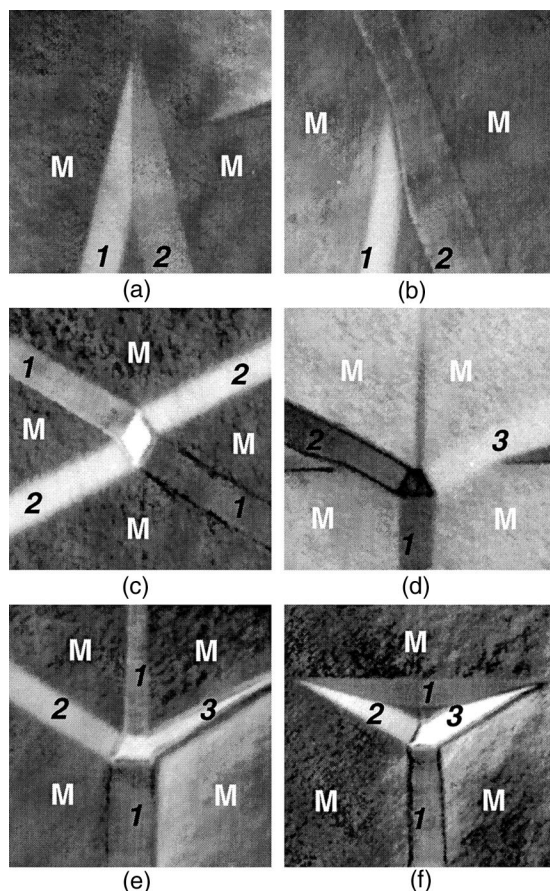


Fig. 9. Typical patterns observed in the Ti-31.25Al-18.75Nb (at%) alloy. *M* stands for the α_2 matrix, 1-3 for the three pairs of orientation variants of the *O*-phase.

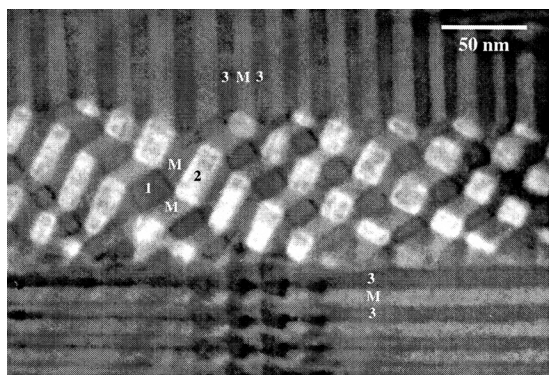


Fig. 10. TEM micrograph of a Ti-Al-Nb alloy with higher volume fraction of the *O*-phase. *M* represents α_2 and 1-3 the three pairs of orientation variants of the *O*-phase. The arrangement of the two variants of the *O*-phase in the central region forms the chess-board-like pattern.

are rotated with respect to each other by multiples of 30° . This explains why the three pairs of orientation variants in the alloy of high volume fraction of the *O*-phase (Fig. 3) favor the shape of a rectangle because it is bounded by invariant planes. By forming

those collective patterns shown in Fig. 4, the elastic energy of the system could be further minimized.

In the case with lower volume fraction of the *O*-phase (Figs 5 and 6), the same principle should also apply (e.g. see those variants enclosed by white circles in Fig. 5(b)). However, the dominant morphology of a variant here is a thin plate. Most of the thin plates end up with a sharp tip (Fig. 5(d)) sharing a common interface with another variant like those illustrated in Fig. 6(b) and (c). As a result, it introduces two types of interfaces, i.e. those between domain/matrix and domain/domain. As can be seen from Fig. 7(b), the strain-free orientations of the domain/domain interfaces are also rotated with respect to each other by multiples of 30° and they were determined to be $\{110\}_O$ and $\{130\}_O$ planes [13]. Those orientations for the two types of interfaces illustrated by dashed lines in Fig. 7(b) and (c) coincide if we rotate one set (each with six members) with respect to the other by $\sim 15^\circ$. This is the origin of the pattern shown in Fig. 4(b) where two variants 30° rotated with respect to each other are evenly separated by a midrib (domain/domain interface) leaving the tips of each variant at an angle of approximately 15° . For the pattern shown in Fig. 4(c), it is basically the same but the tip of the central variant is 30° spread due to the fact that it is accommodated by two domain/domain interfaces on both sides. The above analysis can be extended in a similar way to explain those more complicated patterns shown in Fig. 4(d), (f) and (g) where two types of interfaces coexist.

It should be pointed out that only homogeneous nucleation is considered and the nucleation density is assumed to be very high in our simulations. The morphological evolution may follow different paths if heterogeneous nucleation is the prevailing mechanism or the nucleation density is relatively low. Corresponding studies with controlled nucleus density are underway.

5. SUMMARY

A phase-field model was developed to simulate the precipitation process of orthorhombic (*O*-phase) phase particles from a hexagonal (α_2) matrix in the Ti-Al-Nb alloy system. Two alloy compositions were considered to examine the influence of volume fraction of the *O*-phase on the microstructure. Our simulation demonstrates that in the alloy with a higher volume fraction of the *O*-phase the morphology of the precipitates will be mainly rectangle/square shapes on the (0001) plane of the α_2 phase. These rectangle/square precipitates contact each other at their corners, forming various self-accommodating patterns. In the alloy with lower volume fraction of the *O*-phase, the dominant morphology for the precipitate is thin plates and their mutual arrangement also leads to a number of unique patterns. The morphology of an individual precipitate and those unique patterns formed by collective

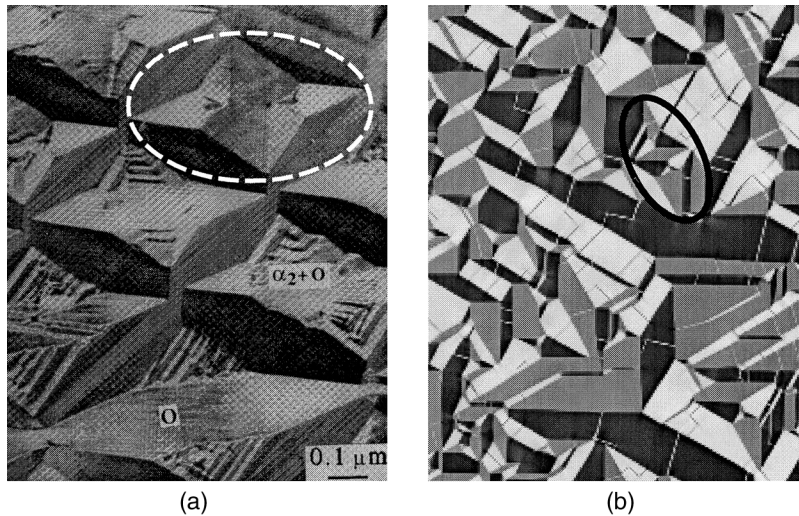


Fig. 11. (a) Microstructural pattern observed on aging at 973 K [11]. (b) Simulated morphological pattern at $\tau = 300$ with 25.0 at%Nb as the mean composition of the Ti–Al–Nb alloy.

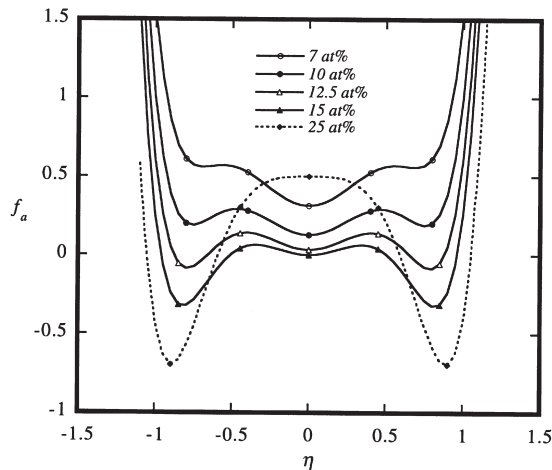


Fig. 12. Plot of local specific free energy against one lro parameter for different representative content of Nb.

arrangement of several orientation variants of precipitates agree remarkably well with experimental observations. All the inter-phase and inter-variant interfaces are found to be invariant planes which minimize the elastic energy.

Acknowledgements—We would like to thank Professor A.G. Khachaturyan and Professor S.A. Dregia for useful discussions. We are grateful for the financial support from ONR under grant number N00014-95-1-0577 (Wen and Chen) and from NSF under grant DMR-9703044 (Wen and Wang) and DMR-96-33719 (Chen). The simulation was performed at the San Diego Supercomputer Center and the Pittsburgh Super-computing Center.

REFERENCES

- Banerjee, D., Gogia, A. K., Nandy, T. K. and Muraleedharan, K., in *Structural Intermetallics*, eds. R. Darolia, J. J. Lewandowski, C. T. Liu, P. L. Martin, D. B. Miracle and M. V. Nathal. Metallurgical Society of AIME, Warrendale, USA, 1993, p. 19.
- Kattner, U. R. and Boettinger, W. J., *Mater. Sci. Engng*, 1992, **A152**, 9.
- Sastry, S. M. L. and Lipsitt, H. A., *Met. Trans.*, 1977, **8A**, 1543.
- Banerjee, D., Gogia, A. K., Nandi, T. K. and Joshi, V. A., *Acta metall.*, 1988, **36**, 871.
- Strychor, R., Williams, T. C. and Soffa, W. A., *Met. Trans.*, 1988, **19A**, 1321.
- Kestner-Weykamp, H. T., Ward, C. H., Broderick, T. F. and Kaufman, M. J., *Scripta metall.*, 1989, **23**, 1697.
- Muraleedharan, K., Gogia, A. K., Nandi, T. K., Banerjee, D. and Lele, S., *Met. Trans.*, 1992, **23A**, 401.
- Muraleedharan, K., Nandi, T. K., Banerjee, D. and Lele, S., *Met. Trans.*, 1992, **23A**, 417.
- Bendersky, L. A., Roytburd, A. and Boettinger, W. J., *J. Res. Natl. Inst. Stand. Technol.*, 1993, **98**, 561.
- Bendersky, L. A. and Boettinger, W. J., *J. Res. Natl. Inst. Stand. Technol.*, 1993, **98**, 585.
- Muraleedharan, K. and Banerjee, D., *Scripta metall.*, 1993, **29**, 527.
- Muraleedharan, K. and Banerjee, D., *Phil. Mag. A*, 1995, **71**, 1011.
- Pierron, X., De Graef, M. and Thompson, A. W., *Phil. Mag. A*, 1998, **77**, 1399.
- Wen, Y.H., Wang, Y. and Chen, L.Q., *Phil. Mag. A*, 2000, **80**, 1967.
- Wen, Y. H., Wang, Y. and Chen, L. Q., *Acta mater.*, 1999, **47**, 4375.
- Lifshitz, E. M. and Pitaevskii, L. P., *Statistical Physics*. Pergamon Press, Oxford, 1980.
- Izyumov, Yu. A. and Syromyatnikov, V. N., *Phase Transitions and Crystal Symmetry, Fundamental Theories of Physics*. Kluwer Academic Publishers, New York, 1990.
- Wang, Y., Chen, L. -Q. and Khachaturyan, A. G., *J. Am. Ceram. Soc.*, 1996, **79**, 987.
- Fan, D. and Chen, L. -Q., *J. Am. Ceram. Soc.*, 1995, **78**, 769.
- Khachaturyan, A. G., *Theory of Structural Transformations in Solids*. John Wiley & Sons, New York, 1983.
- Chen, L. Q. and Shen, J., *Comput. Phys. Comm.*, 1998, **108**, 147.
- Le Bouar, Y., Loiseau, A. and Khachaturyan, A. G., *Acta metall.*, 1998, **46**, 2777.
- Bendersky, L. A. and Boettinger, W. J., *Acta mater.*, 1994, **42**, 2337.